

Experimental evidence for a current-biased Josephson junction acting as either a macroscopic boson or fermion

P. H. Ouyang,¹ S. R. He,¹ Y. Z. Wang,¹ Y. Q. Chai,¹ J. X. He,¹ H. Chang,² and L. F. Wei^{1,*}

¹Information Quantum Technology Laboratory, International Cooperation Research Center of China Communication and Sensor Networks for Modern Transportation, School of Information Science and Technology, Southwest Jiaotong University, Chengdu 610031, China

²Qixing Vacuum Coating Technology Co., Ltd., Chengdu 610031, China

 (Received 29 August 2023; revised 10 January 2024; accepted 7 February 2024; published 4 March 2024)

It is well known that elementary particles in the real 3 + 1-dimensional world are either bosons or fermions, without exception, and not both. Here, we show that a quantized current-biased Josephson junction (CBJJ), as an artificial macroscopic “particle,” can serve as either a boson or a fermion or the combination, depending on the amplitude of the biased dc current. By using high vacuum two-angle electron beam evaporations, we fabricated CBJJ devices and calibrated their physical parameters by applying low-frequency signal drivings. At 50 mK temperature environment, the microwave transmission characteristics of the fabricated CBJJ devices were measured at the low power limit. The experimental results verify the relevant theoretical predictions, i.e., when the bias current is significantly lower than the critical ones of the junctions, the device works in a very linear regime and thus behaves as a harmonic oscillator “boson”; while if the biased current is sufficiently large (especially approaching the junctions’ critical currents), the device works manifestly in the nonlinear regime and thus behaves as a two-level artificial atom “fermion.” Therefore, by adjusting the biased dc current, the CBJJ device can be effectively switched from a Bose-type macroscopic particle to a Fermi-type one and thus might open an approach for quantum technology applications at a macroscopic scale.

DOI: [10.1103/PhysRevResearch.6.013236](https://doi.org/10.1103/PhysRevResearch.6.013236)

I. INTRODUCTION

Spin quantum statistics, related to the well-known Pauli exclusion principle, is one of the basic features in quantum mechanics [1]. In three-dimensional space, microscopic particles have either integer or half-integer spin quantum numbers and thus can be divided into the bosons and fermions, respectively. Phenomenologically, the boson-type particles (such as photons and phonons) obey the Bose-Einstein statistics and the relevant bosonic creation and annihilation operators, \hat{a}^\dagger and \hat{a} , satisfy the bosonic commutation relation $[\hat{a}, \hat{a}^\dagger] = \hat{a}\hat{a}^\dagger - \hat{a}^\dagger\hat{a} = 1$; while the fermion-type particles (such as electrons) obey the Fermi-Dirac statistics, whose creation and annihilation operators, \hat{b}^\dagger and \hat{b} , satisfy the anticommutation relation $\{\hat{b}, \hat{b}^\dagger\}_+ = \hat{b}\hat{b}^\dagger + \hat{b}^\dagger\hat{b} = 1$. Basically, all objects called elementary particles in the real 3 + 1-dimensional world are either bosons or fermions, without exception, and not both.

However, in two-dimensional space certain “particles” can lie somewhere between the bosons or fermions [2], e.g., anyons. For example, the elementary excitations of fractional quantum Hall effect systems at filling factor $\nu = 1/m$ (with

m being an odd integer) have been predicted to obey Abelian fractional statistics, which were detected recently by measuring the current correlations of the collision between anyons (with the filling factor $\nu = 1/3$) at a beamsplitter [3]. The non-Abelian anyons [4], which were just verified indirectly [5,6], are particularly desired for fault-tolerant quantum computation [7]. A natural question is, are the statistical behaviors of three-dimensional macroscopic artificial objects, working in different parameter regimes, still controllable? If so, then the different applications based on their mutually exclusive statistical features could be realized with such devices. For example, if certain elementary devices could be manipulated as either bosons sometimes or fermions at the other times, then their controllability could be significantly improved in compact solid-state circuits on a chip [8].

In fact, a single bosonic Josephson junction, implemented by two weakly linked Bose-Einstein condensates in a double-well potential, has been experimentally realized [9]. Also, it has been shown that under the low-excitation limit, a Josephson junction with a small dc-current bias could be effectively treated as a linear harmonic oscillator [10], which can quantized as a simple-mode boson and thus could serve as the quantum data bus to implement the couplings between distant superconducting qubits. If the biased dc current is sufficiently large (e.g., approaching its critical current), the quantized CBJJ device has only a few bound states [11] and thus can be treated as a macroscopic qubit (i.e., a fermion), called the CBJJ qubit [12], for superconducting quantum information computing [13]. This implies that a current-biased Josephson junction (CBJJ), acting as an artificially macroscopic quantum

*Corresponding author: lfwei@swjtu.edu.cn

Published by the American Physical Society under the terms of the Creative Commons Attribution 4.0 International license. Further distribution of this work must maintain attribution to the author(s) and the published article’s title, journal citation, and DOI.

system, can serve as either a boson or a fermion, depending on its biased current.

In this work we provide directly the experimental evidence that a CBJJ device is really a combination of the macroscopic boson and fermion objects, i.e., it can work as either a boson or a fermion under the extreme dc-current biases, and as both of them for the other-biased regime. First, by using the standard input-output theory, we predict the microwave scattering features of the device with the two extreme biases; one is to generate a boson, and the other is to generate a fermion. Next, the device is fabricated and then measured under low-power microwave drivings at ultralow temperature. The experimental results agree well with the corresponding theoretical predictions, i.e., the quantized CBJJ device can serve as either a macroscopic boson for a relatively low dc-current bias or a macroscopic fermion under a sufficiently large dc-current bias, under the low-excitation limit. Between these biases, the device works as a boson with certain probabilities and also as a fermion with other probabilities. With these theoretical predictions and also the experimental verifications, a superconducting circuit to implement macroscopic quantum information processing might be constructed, wherein the quantized CBJJ devices play double roles: their fermionic behaviors can be utilized to encode the CBJJ qubits, and their bosonic features can serve as the data buses to implement the indirect coupling between distant qubits and the high fidelity readouts of solid-state qubits.

II. MODELS AND EXPERIMENTAL PREDICTIONS

We first develop a theoretical approach to confirm that a quantized CBJJ device, under the different dc-current biases, can serve as either a macroscopic boson or a macroscopic fermion. These predictions will be verified experimentally later.

A. Macroscopic quantum bound states of a current-biased Josephson Junction

As a macroscopic quantum device, the phase δ dynamics of a CBJJ shown in Fig. 1 is equivalent to that of a particle with the mass $C_J[\Phi_0/(2\pi)]^2$ (with C_J being the effective capacitance of the junction) moving in a potential [11, 14]:

$$U(\delta) = \frac{I_c \Phi_0}{2\pi} \left(-\frac{I_b}{I_c} \delta - \cos \delta \right) = -E_J \left(\frac{I_b}{I_c} \delta + \cos \delta \right),$$

where $\Phi_0 = h/(2e) = 2.07 \times 10^{-15}$ Wb is the flux quanta, $\delta = 2\pi\phi/\Phi_0$ is the gauge invariant phase across the junction, ϕ is the flux, $I_b (< I_c)$ is the biased dc current; I_c and $E_J = 2\pi I_c/\Phi_0$ are the critical current and Josephson energy of the junction, respectively. It is seen that this wash potential contains a series of potential traps, whose lowest and highest potentials are determined by

$$\left. \frac{dU(\delta)}{d\delta} = -E_J \left(\frac{I_b}{I_c} - \sin \delta \right) \right|_{\delta=\delta_{\min}, \delta_{\max}} = 0,$$

with $d^2U(\delta)/d\delta^2|_{\delta=\delta_{\min}} > 0$ and $d^2U(\delta)/d\delta^2|_{\delta=\delta_{\max}} < 0$, respectively.

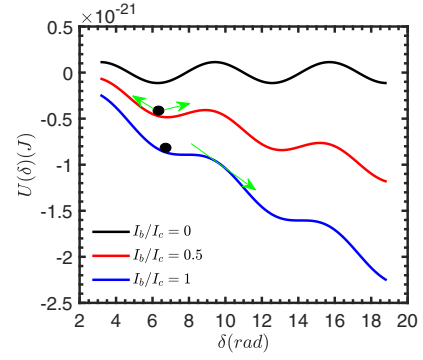


FIG. 1. Under the dc-biased current $I_b < I_c$, the CBJJ is equivalent to a macroscopic phase particle with the mass m moving in a wash potential, which contains a series of potential traps with the limited heights $\Delta U = U_{\max} - U_{\min}$. Here, the black ball indicates to the phase particle, which moves in the trap with the plasma frequency ω_p , and the junction parameters are set as $I_c = 0.975 \mu\text{A}$, $C_J = 93 \text{ fF}$.

It is easily proved that

$$\begin{aligned} \delta_{\min} &= 2k\pi + \sin^{-1} \left(\frac{I_b}{I_c} \right), \\ \delta_{\max} &= (2k + 1)\pi - \sin^{-1} \left(\frac{I_b}{I_c} \right), \end{aligned}$$

with $k = 0, 1, 2, \dots$. For example, between $\delta = \pi$ and $\delta = 3\pi$, we have the local minimal potential U_{\min} at $\delta_{\min} = 2\pi + \sin^{-1}(I_b/I_c)$ and the local maximal one U_{\max} at $\delta_{\max} = 3\pi - \sin^{-1}(I_b/I_c)$. Of course, if $I_b \geq I_c$, the Josephson junction just behaves as a normal-state resistor R_n and thus generates a nonzero voltage signal under such a current bias. Near the bottom of the potential trap, i.e., $\delta \sim \delta_{\min}$, the local potential of the phase particle can be expressed as

$$\begin{aligned} U(\delta) &= U(\delta_{\min}) + \frac{1}{2} \frac{d^2U(\delta)}{d\delta^2} (\delta - \delta_{\min})^2 + \dots \\ &\approx \frac{1}{2} m\omega_p^2 (\delta - \delta_{\min})^2, \end{aligned} \quad (1)$$

with the plasma frequency [15]

$$\omega_p(I_b) = \omega_p \sqrt{1 - \left(\frac{I_b}{I_c} \right)^2},$$

where $\omega_p = \sqrt{2\pi I_c/\Phi_0 C_J}$ is the plasma frequency for $I_b = 0$. Mathematically, the height of the local potential trap can be calculated as

$$\begin{aligned} \Delta U &= U(\delta_{\max}) - U(\delta_{\min}) \\ &= 2E_J \left(\sqrt{1 - \left(\frac{I_b}{I_c} \right)^2} - \left(\frac{I_b}{I_c} \right) \cos^{-1} \left(\frac{I_b}{I_c} \right) \right), \end{aligned} \quad (2)$$

which is controllable by adjusting the amplitude of the biased dc current I_b .

At ultralow temperatures (50 mK), the quantized CBJJ device can be described by a junction capacitance C_J parallel to a nonlinear inductance L_J , and thus it can be described by

TABLE I. Energy differences between the nearest-neighbor levels of the lower bound states $|n\rangle$ of the CBJJ and their “dipole-transition” matrix elements $\delta_{nm} = \langle n|m\rangle$ for the typical biased relative currents I_b/I_c . Here, $C_J = 93$ fF, $\omega_{nm}/2\pi = (E_m - E_n)/\hbar$, $n \neq m = 0, 1, 2, 3$, and the unit of $\omega_{nm}/2\pi$ in the table is GHz.

I_b/I_c	$\omega_{01}/2\pi$	$\omega_{12}/2\pi$	$\omega_{23}/2\pi$	δ_{01}	δ_{12}	δ_{23}
0.000	2.5950	2.5940	2.5937	0.052	0.073	0.090
0.450	2.5912	2.5904	2.5899	0.055	0.077	0.097
0.680	2.5775	2.5719	2.5683	0.060	0.085	0.105
0.945	2.5072	2.4042	2.2724	0.091	0.130	0.158
0.955	2.4616	2.3030	2.0556	0.095	0.134	0.163
0.964	2.4390	2.1266		0.101	0.141	
0.970	2.4184			0.106		

a quantized Hamiltonian [11]:

$$\hat{H}_{\text{CBJJ}} = \frac{\hat{p}_\delta^2}{2C_J \left(\frac{\Phi_0}{2\pi}\right)^2} + U(\delta). \quad (3)$$

The macroscopic bound states with a series of discrete levels can be obtained by solving the following stationary Schrödinger equation:

$$\hat{H}_{\text{CBJJ}}|n\rangle = E_n|n\rangle, \quad n = 0, 1, 2, \dots$$

Specifically, for $C_J = 93$ fF Table I lists the corresponding transition frequencies and the “dipole-transition” matrix elements between the neighbor stationary states with the lower energies, under the typical biased currents, e.g., $I_b/I_c = 0, 0.45, 0.68, 0.945, 0.955, 0.964$, and 0.97 , respectively. It is seen that, for sufficiently low biased current, the energy differences between the lower macroscopic bound states in the potential trap are almost the same, with almost equivalent “dipole-transition” probabilities. For sufficiently large biased currents, the number of the macroscopic bound states in the potential trap are very limited and the relevant energy difference, as well as the “dipole-transition” probabilities, between them are significantly different. Specifically, Fig. 2 shows how these behaviors change with the biased dc current.

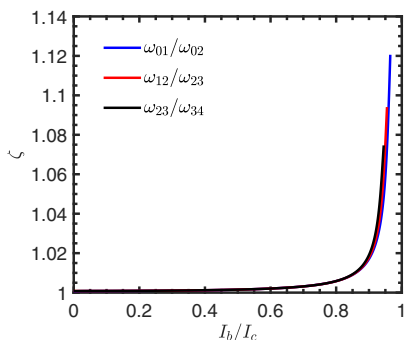


FIG. 2. The ratio $\zeta = \omega_{nm}/\omega_{mk}$, $n = 0, 1, 2$, $m = n + 1$, $k = m + 1$, of the transition frequencies between the nearest-neighbor bound states of the CBJJ versus the biased current. Here, the relevant parameters are set as $I_c = 0.975$ μA , $C_J = 93$ fF. Note that here just three, four, and five bound states are allowed for $I_b/I_c \leq 0.965$, 0.957 , and 0.951 , respectively.

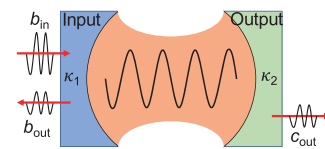


FIG. 3. A configuration of the traveling-wave photons scattered by the CBJJ, working as a macroscopic boson (i.e., a simple-mode cavity). Here, \hat{b}_{in} and \hat{b}_{out} are the amplitudes of the photons in and out of the CBJJ, and \hat{c}_{out} is that of the right-side photon.

The above numerical results imply that, under low-power driving, a CBJJ with sufficiently low bias current can work as a linear harmonic oscillator, whose coherence time could be sufficiently long (due to the relatively low biased current noise). In this case, the Hamiltonian of the quantized CBJJ device can be expressed as [10]

$$\hat{H}_b \approx \frac{1}{2m_J} \hat{p}_\theta^2 + \frac{1}{2} m_J \omega_p^2 (I_b) \hat{\theta}^2 = \hbar \omega_p (I_b) \left(\hat{a}_p^\dagger \hat{a}_p + \frac{1}{2} \right), \quad (4)$$

where $\hat{\theta} = \hat{\delta} - \delta_{\text{min}}$, and \hat{a}_p and \hat{a}_p^\dagger are the I_b -dependent bosonic annihilation and creation operators, respectively. If the biased dc current is sufficiently large, which yields the significantly strong nonlinearity, then the quantized CBJJ device should serve as an artificial atom with the transition between the bound states possessing well selectivity, due to the manifest difference between the transition frequencies. For example, under the limit $I_b \lesssim I_c$, the lowest two levels of the quantized CBJJ device could be utilized to encode a CBJJ qubit with the Hamiltonian [12]

$$H_f \approx \frac{\hbar \omega_{01}(I_b)}{2} \sigma_z, \quad (5)$$

where $\sigma_z = |1\rangle\langle 1| - |0\rangle\langle 0|$ is the Pauli-type fermionic operator, satisfying the communication relation $[\sigma_z, \sigma_\pm] = \pm 2\sigma_\pm$, $[\sigma_+, \sigma_-] = \sigma_z$, with $\sigma_+ = |1\rangle\langle 0|$ and $\sigma_- = |0\rangle\langle 1|$.

Obviously, under the low-excitation limit, the quantized CBJJ device can work as either a macroscopic boson or a macroscopic fermion, depending on its different dc-current biases for the controllable eigenfrequency. This is an interesting feature for a macroscopic object, and thus it is desirable to test it both theoretically and experimentally.

B. Transport properties of the low-power traveling-wave photons scattered by the CBJJ device under different biases

To theoretically confirm the above argument that a quantized CBJJ can serve as either a boson or a fermion, let us investigate the scattering properties of the traveling-wave photon transported along a transmission line.

First, if the CBJJ serves as a boson, which is physically equivalent to a quantized bosonic mode of a cavity, then the configuration shown in Fig. 3 can be utilized to describe the transport properties of the traveling-wave photons scattered by the CBJJ. The Hamiltonian of the present system can be expressed as $\hat{H}_B = \sum_{l=b,c} \hat{H}_l + H_{\text{CBJJ}} + \hat{H}_{\text{CBJJ-TL}}$, where

$$\hat{H}_l = \int d\omega \sum_{l=b,c} \hbar \omega \hat{l}^\dagger(\omega) \hat{l}(\omega) \quad (6)$$

describes the traveling-wave microwave photon transported along the transmission line with $l = b, c$ referring to its left and right sides, and the relevant bosonic operators satisfy the commutation relation: $[l(\omega), l^\dagger(\omega')] = \delta(\omega - \omega')$. Also, the flux operator of the traveling-wave photon reads [14–16]

$$\hat{\phi}_l(x) = \sqrt{\frac{\hbar Z_0}{4\pi}} \int_0^\infty \frac{d\omega}{\sqrt{\omega}} [\hat{l}(\omega)e^{ikx} + \hat{l}^\dagger(\omega)e^{-ikx}], \quad (7)$$

with Z_0 being the characteristic impedance of the transmission line, and thus

$$\dot{\hat{\phi}}_l(x) = (-i)\sqrt{\frac{\hbar Z_0}{4\pi}} \int_0^\infty d\omega \sqrt{\omega} [\hat{l}(\omega)e^{ikx} - \hat{l}^\dagger(\omega)e^{-ikx}]. \quad (8)$$

Under a sufficiently low current bias, the CBJJ Hamiltonian reads $\hat{H}_{\text{CBJJ}} \approx \hat{H}_b$, shown in Eq. (4). The physical boundary condition at $x = 0$, i.e., the location of the device, reads $\hat{l}(0_b, t) = \hat{l}(0_c, t)$, $V_J = (\Phi_0/2\pi)\dot{\delta} + [\dot{\phi}(0_b) - \dot{\phi}(0_c)]$. Thus, under the low-excitation limit and rotating-wave approximation, i.e., the photon scattering is the desired elastic type and any possibly created and annihilated photons at $x = 0$ are neglected, we have

$$\begin{aligned} \hat{H}_{\text{CBJJ-B}} &= C_J \hat{p}_\theta [\dot{\phi}(0_b) - \dot{\phi}(0_c)] \\ &= i\hbar \sqrt{\frac{\kappa_l}{2\pi}} \int d\omega [a^\dagger l(\omega) - l^\dagger(\omega)a], \end{aligned}$$

where $\kappa_l = Z_0/4Z_J$ ($l = b, c$) describes the interaction between the CBJJ and the left/right traveling-wave photons, $Z_J = \sqrt{L_J/C_J}$ is the characteristic impedance of the Josephson junction. As a consequence, the Hamiltonian (with $\hbar = 1$) of the system [16–18] is

$$\begin{aligned} H_B &= \left(\omega_p - \frac{i\gamma}{2}\right) a^\dagger a \\ &+ \int d\omega \left[\omega b(\omega)^\dagger b(\omega) + i\sqrt{\frac{\kappa_1}{2\pi}} [a^\dagger b(\omega) - ab(\omega)^\dagger] \right] \\ &+ \int d\omega \left[\omega c(\omega)^\dagger c(\omega) + i\sqrt{\frac{\kappa_2}{2\pi}} [a^\dagger c(\omega) - ac(\omega)^\dagger] \right], \end{aligned} \quad (9)$$

where γ is decay rate of the cavity, and κ_1 and κ_2 are the effective strengths of the boson coupled to the photons in the left and right sides of the transmission line, respectively. By using the standard input-output theory [18,19], we get the relations

$$\frac{da}{dt} = \left(-i\omega_p - \frac{\kappa + \gamma}{2}\right)a + \sqrt{\kappa_1}b_{\text{in}}(t) + \sqrt{\kappa_2}c_{\text{in}}(t) \quad (10)$$

and

$$\frac{da}{dt} = \left(-i\omega_p + \frac{\kappa - \gamma}{2}\right)a - \sqrt{\kappa_1}b_{\text{out}}(t) - \sqrt{\kappa_2}c_{\text{out}}(t), \quad (11)$$

with $\kappa = \kappa_1 + \kappa_2$, and

$$\hat{b}_{\text{in/out}} = \pm \frac{1}{\sqrt{2\pi}} \int d\omega e^{-i\omega(t-t')} b_0(\omega)$$

and

$$\hat{c}_{\text{in/out}} = \pm \frac{1}{\sqrt{2\pi}} \int d\omega e^{-i\omega(t-t')} c_0(\omega),$$

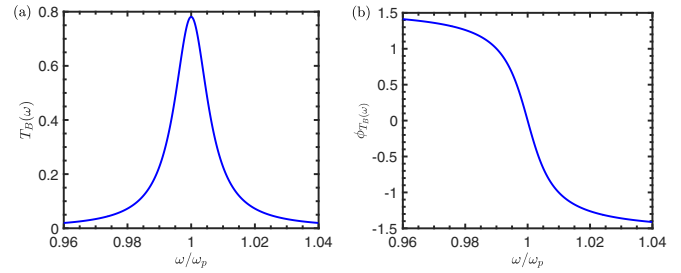


FIG. 4. The transmitted spectrum (a) and phase shift spectrum (b) of the traveling wave scattered by the CBJJ. Here, the relevant parameters are set as $\kappa_1 = 0.004$, $\kappa_2 = 0.008$, $\gamma = 0.0008$, and $\omega_p/2\pi = 2.595$ GHz.

are the input- and output fields, respectively. After the Fourier transformation, $x(t) = \int_{-\infty}^{+\infty} e^{-i\omega(t-t_0)} x(\omega) d\omega / \sqrt{2\pi}$, for $x(t) = a(t)$, $b_{\text{in}}(t)$, $c_{\text{in}}(t)$, $b_{\text{out}}(t)$, and $c_{\text{out}}(t)$, respectively, we have

$$\begin{aligned} -i\omega a(\omega) &= \left(-i\omega_p - \frac{\kappa - \gamma}{2}\right)a(\omega) \\ &+ \sqrt{\kappa_1}b_{\text{in}}(\omega) + \sqrt{\kappa_2}c_{\text{in}}(\omega) \end{aligned} \quad (12)$$

and

$$\begin{aligned} -i\omega a(\omega) &= \left(-i\omega_p + \frac{\kappa + \gamma}{2}\right)a(\omega) \\ &- \sqrt{\kappa_1}b_{\text{out}}(\omega) - \sqrt{\kappa_2}c_{\text{out}}(\omega). \end{aligned} \quad (13)$$

For the configuration shown in Fig. 4, we can assume that $c_{\text{in}}(t) = 0$. Consequently, we have

$$\begin{aligned} b_{\text{in}}(\omega) + b_{\text{out}}(\omega) &= \sqrt{\kappa_1}a(\omega), \\ c_{\text{in}}(\omega) + c_{\text{out}}(\omega) &= \sqrt{\kappa_2}a(\omega). \end{aligned} \quad (14)$$

Therefore, the measurable transmitted and phase shift spectra of the traveling-wave photons can be calculated as

$$T_B(\omega) = \left| \frac{c_{\text{out}}(\omega)}{b_{\text{in}}(\omega)} \right|^2 = \frac{4\kappa_1\kappa_2}{4(\omega - \omega_p)^2 + (\kappa + \gamma)^2} \quad (15)$$

and

$$\phi_{T_B}(\omega) = \arctan \left[-\frac{2(\omega - \omega_p)}{\kappa + \gamma} \right], \quad (16)$$

respectively. In Fig. 4 we shows the spectra of the traveling-wave microwave photons scattered by a quantized CBJJ device with the typical parameters: $I_b = 0 \mu\text{A}$, $I_c = 0.975 \mu\text{A}$, $C'_J = 11.18$ pF, and thus $\omega_p/2\pi \sim 2.595$ GHz. It is seen clearly that, if the CBJJ device works as a boson, the peak of the photon transmission is located as the eigenfrequency of the cavity, i.e., $\omega = \omega_p$, while the phase shift of the transmitted photon is zero.

Alternatively, if the CBJJ is biased near its critical current, e.g., $0.965 < I_b/I_c \leq 0.98$, only two macroscopic bound states exist in the relevant local potential, yielding that the CBJJ works effectively as a two-level artificial atom, i.e., a fermion with the Hamilton $\hat{H}_{\text{CBJJ}} \sim \hat{H}_f$ shown in Eq. (5). Similarly, the validity of such an equivalence can be tested by probing the transport properties of the traveling-wave photons scattered by the device under the relevant bias. The generic

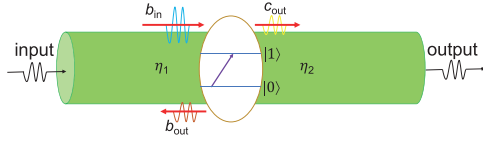


FIG. 5. A configuration of the traveling-wave photon scattered by a two-level atom, i.e., a fermion.

model, shown schematically in Fig. 5, to describe the photon transport scattered by a two-level atom, i.e., a fermion, generated by the present CBJJ, can be described by the Hamiltonian [20]

$$\begin{aligned}
 H_F = & \left(\omega_{01} - \frac{i\Gamma}{2} \right) \sigma_z \\
 & + \int d\omega \left[\omega b(\omega)^\dagger b(\omega) + \sqrt{\frac{\eta_1}{2\pi}} (\sigma_+ b(\omega) - b(\omega)^\dagger \sigma_-) \right] \\
 & + \int d\omega \left[\omega c(\omega)^\dagger c(\omega) + \sqrt{\frac{\eta_2}{2\pi}} (\sigma_+ c(\omega) - c(\omega)^\dagger \sigma_-) \right]
 \end{aligned} \quad (17)$$

with ω_0 and ω_1 being the eigenfrequencies of the bound states $|0\rangle$ and $|1\rangle$, respectively. $\eta_{1,2} = (2\pi\lambda/\Phi_0)^2 Z_0/2\hbar$ is the effective strength of the fermion coupled to the photon in the left and right transmission lines. It is easy to get the Heisenberg equations for the traveling-wave photon operators:

$$i \frac{db(\omega)}{dt} = \omega b(\omega) + \sqrt{\frac{\eta_1}{2\pi}} \sigma_-, \quad (18)$$

$$i \frac{dc(\omega)}{dt} = \omega c(\omega) + \sqrt{\frac{\eta_2}{2\pi}} \sigma_-; \quad (19)$$

and the two-level atomic operator σ_- :

$$\begin{aligned}
 i \frac{d\sigma_-}{dt} = & \left(\omega_{01} - \frac{i\gamma}{2} \right) \sigma_- - \sqrt{\frac{\eta_1}{2\pi}} \int d\omega \sigma_z b(\omega) \\
 & - \sqrt{\frac{\eta_2}{2\pi}} \int d\omega \sigma_z c(\omega).
 \end{aligned} \quad (20)$$

Defining again the in and out operators,

$$\hat{b}_{\text{in/out}} = \mp \frac{1}{\sqrt{2\pi}} \int d\omega e^{-i\omega(t-t')} b_0(\omega)$$

and

$$\hat{c}_{\text{in/out}} = \mp \frac{1}{\sqrt{2\pi}} \int d\omega e^{-i\omega(t-t')} c_0(\omega),$$

of the traveling-wave photon scattered by the fermion and using again the standard input-output theory, we get the following input-output relations:

$$\begin{aligned}
 \frac{d\sigma_-}{dt} = & \left(-i\omega_{01} - \frac{\eta + \gamma}{2} \right) \sigma_-(t) \\
 & + i\sqrt{\eta_1} \sigma_z b_{\text{in}}(t) + i\sqrt{\eta_2} \sigma_z c_{\text{in}}(t)
 \end{aligned} \quad (21)$$

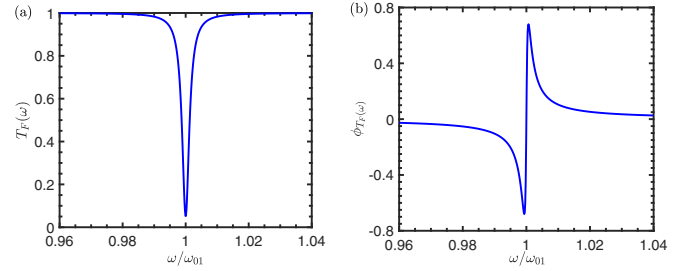


FIG. 6. The transmitted (a) and phase shift (b) spectra of the traveling-wave photons scattered by a fermion generated by the CBJJ device. Here, the relevant parameters are set as $\eta = 0.0021$, $\gamma = 0.0062$, and $\omega_{01}/2\pi = 2.42$ GHz.

and

$$\begin{aligned}
 \frac{d\sigma_-}{dt} = & \left(-i\omega_{01} + \frac{\eta - \gamma}{2} \right) \sigma_-(t) \\
 & + i\sqrt{\eta_1} \sigma_z b_{\text{out}}(t) + i\sqrt{\eta_2} \sigma_z c_{\text{out}}(t).
 \end{aligned} \quad (22)$$

Consequently, we have

$$\begin{aligned}
 \sqrt{\eta_1} b_{\text{in}}(t) - \sqrt{\eta_2} c_{\text{out}}(t) &= i\eta \sigma_-(t), \\
 \sqrt{\eta_2} c_{\text{in}}(t) - \sqrt{\eta_1} b_{\text{out}}(t) &= i\eta \sigma_-(t),
 \end{aligned} \quad (23)$$

with $\eta = \eta_1 + \eta_2$. Therefore, the scattering matrix $\langle k'|S|k\rangle$ between the input state $|k\rangle \sim b_{\text{in}}^\dagger|0\rangle$ and the output state $|k'\rangle \sim b_{\text{out}}^\dagger|0\rangle$ of the photons can be expressed as

$$\begin{aligned}
 \langle k'|S|k\rangle &= \frac{1}{\sqrt{2\pi}} \int dt \langle 0|c_{\text{out}}(t)|k^+\rangle \\
 &= t_F(k) \delta(k-p),
 \end{aligned} \quad (24)$$

yielding the amplitude of the photon transmission,

$$t_F(\omega) = \frac{t_F(k) + 1}{2} = \frac{2(\omega - \omega_{01}) + i\Gamma}{2(\omega - \omega_{01}) + i(\eta + \Gamma)}, \quad (25)$$

specifically for $\eta_1 = \eta_2$. Obviously, the transmitted probability and phase shift of the traveling-wave photon can be expressed as

$$T_F(\omega) = |t_F(\omega)|^2 = \frac{4(\omega - \omega_{01})^2 + \gamma^2}{4(\omega - \omega_{01})^2 + (\eta + \gamma)^2} \quad (26)$$

and

$$\phi_{T_F(\omega)} = \arctan \left[-\frac{4(\omega - \omega_{01})^2 + \gamma(\gamma + \eta)}{2\eta(\omega - \omega_{01})} \right], \quad (27)$$

respectively. One can see from Fig. 6 that the peak of the reflected photon takes place at $\omega = \omega_{01}$, i.e., the resonant photon is maximally reflected. Near such a resonant photon, the phase shift of the traveling-wave photon shows a manifestly critical behavior. These features are basically different from those of the boson scattering demonstrated above.

III. EXPERIMENTS AND RESULT ANALYSIS

In this section, we report the experimental tests of the above arguments and the relevant theoretical predictions, by fabricating the devices and measuring their microwave transport properties.

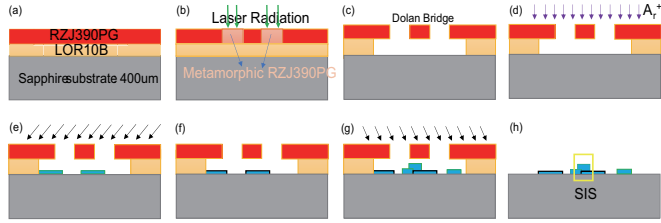


FIG. 7. A simplified process flow for the Josephson junction fabrication: (a) uniform double layer photoresist, (b) exposure, (c) development, (d) ion etching oxide layer, (e) Al by oblique evaporation, (f) oxidation, (g) Al by positive rake angle evaporation, (h) remove the photoresist. The yellow frame refers to the section of the junction area.

A. Device fabrication and its physical parameter measurements

By using the usual electron beam evaporations, the fabricated Josephson junction is embedded in a coplanar waveguide transmission line. Figure 7 shows briefly the process for the fabrication of an Al/AIO_x/Al junction. It mainly includes two steps: preparing a so-called Dolan bridge by laser direct writing lithography, and fabricating the desired “SIS” structure by the oblique deposition of aluminium films and oxidation. The device was fabricated on a 400 µm thick single-side polished sapphire substrate, which is cleaned with acetone and ultrasonic waves. The device structure is generated by using a laser direct-writing lithography process and then the wet etchings. The aluminum film is deposited onto the prepared “Dolan bridge” structure on the sapphire substrate by double-angle electron evaporations in the high vacuum environment. The thicknesses of the fabricated Al/AIO_x/Al junction are estimated as 80 nm for the upper Al film, 1.2 nm for the junction, and 120 nm for the lower Al film. As shown in Fig. 8, the widths of the transmission line and the gap are set as ~10 µm, and the area *A* of the junction is 1.26 µm². Also, the distance between transmission line and the grounded one is set as ~5 µm, to implement the *Z* ≈ 50 Ω wave impedances matching with the external microwave devices.

To extract the physical parameters such as, typically, the effective junction capacitance *C_J*, normal-state resistance *R_N*, the approximated critical current *I_c*, etc. of the fabricated Josephson junction, we first measured the *I-V* characteristic curve of the device by probing the switching currents of the junction, under low-frequency ac drivings. A measurement circuit of the four-terminal method is shown in Fig. 9, wherein the amplitude of the driving current is changed slowly and the voltage across the device is measured by a room temperature amplifier. A low-temperature copper filter and a large room-temperature resistor (whose resistance is much larger than the junction resistance *R_N*) are used to measure the slowly changing current through the junction. At 50 mK, the measured *I-V* curve of the fabricated Josephson junction is shown in Fig. 10(a), which shows that the junction works in the underdamped regime and its normal-state resistance is *R_N* = 290 Ω. Consequently, with the superconducting gap of the Al, Δ = 180 µeV, the critical current of the junction can be estimated roughly as *I_c* = 0.975 µA, according to the Ambegaokar-Baratoff formula [21], *I_c* = πΔ/(2e*R_N*). On the other hand, the three-layer structure of the SIS junction can

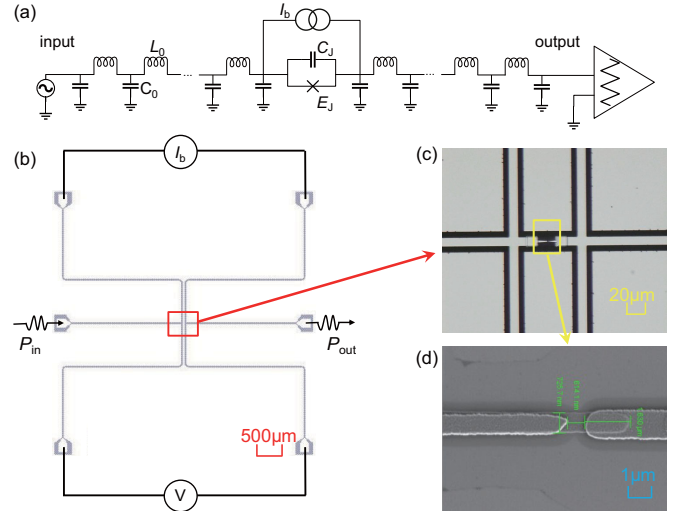


FIG. 8. The fabricated CBJJ device: (a) Its equivalent circuit. (b) The device structure, wherein the left wire connects the dc-current source, the right wire is used to measure the voltage across the junction, and the low-power traveling-wave microwave is driven along the middle transmission line. (c) A microscope image of the junction marked in the red box. (d) A scanning electron microscope image of the fabricated junction (in the orange box, with the area being 1.26 µm²).

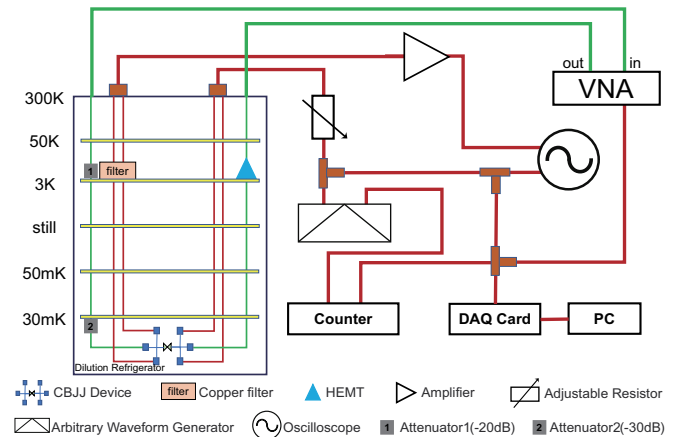


FIG. 9. The circuit to measure the *I-V* characteristic curve of the fabricated Josephson junction under low-frequency ac driving.

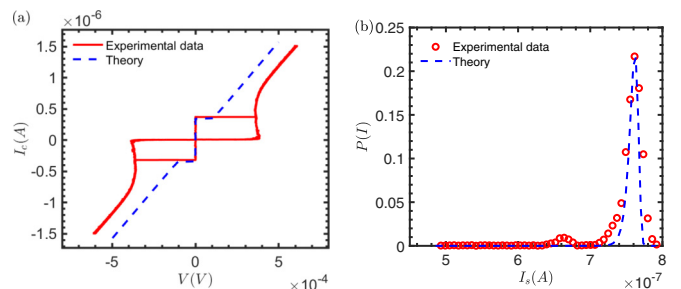


FIG. 10. Low-frequency driving measurements of a fabricated Josephson junction. (a) The *I-V* curve, from which we know that the normal-state resistance of the junction is *R_N* = 290 Ω. (b) The jump current measurements, wherein the junction is switched from the zero voltage state to the nonzero voltage state if the bias current is *I_s*.

be treated as a parallel plate capacitor, as it is composed of two superconductors separated by a thin insulating layer. Therefore, the capacitance of the junction can be phenomenologically calculated as $\tilde{C}_J = \epsilon_r \epsilon_0 A / d \approx 93$ fF, with the area of the junction being $A \approx 1.26 \mu\text{m}^2$, the thickness of the barrier layer being $d \approx 1.2$ nm, and the vacuum permittivity and the relative permittivity of AlO_x being $\epsilon_0 = 10^{-12}$ F/m and $\epsilon_r = 10$ F/m, respectively. However, as the junction is not an isolated device, it is realistically integrated with the other devices on a chip, the effectively physical parameters should be determined by the relevant experimental measurements, and then simulated by the corresponding theoretical model such as the generic RCSJ model described by the following dynamical equation [15]:

$$I_b = \frac{\hbar C_J}{2e} \frac{d^2 \delta}{dt^2} + \frac{\hbar}{2e R_N} \frac{d\delta}{dt} + I_c \sin \delta, \quad (28)$$

where C_J and I_c are the effective capacitance and critical current of the junction, I_b is its low-frequency bias current (which is a sawtooth wave with frequency $f = 71.3$ Hz and amplitude $I_{pp} = 3 \mu\text{A}$, generated by an arbitrary waveform generator, Agilent 33250A), and I_n the noise current (typically from, e.g., thermal fluctuation). First, the synchronization signal is triggered at zero time as the start timing. Then, a slowly increasing bias current (with the slope being $dI/dt = 190$ A/s) is applied to the junction monitored by a voltage signal; when the voltage across the junction switches from zero to a threshold nonzero value, the timing is ended and the bias current at this time is recorded as the jump current I_s . After repeated such a switch measurement with $N = 10\,000$ times, we get a statistical distribution of the measured jump currents $P(I_s)$, shown in Fig. 10(b). It is seen that the maximal jump current is $\approx 0.78 \mu\text{A}$, which is certainly less than the effective critical current of the junction. With the simulations based on the RCSJ model, whose parameters are numerically adjustable, the experimentally measured statistical distribution of the jump current is well fitted by the blue line in Fig. 10(b), from which the effective capacitance and critical current of the junction can be extracted as $C_J = 93$ fF and $I_c = 0.979 \mu\text{A}$, respectively.

B. Low-power microwave transport measurements

With the fabricated CBJJ device whose physical parameters have been calibrated experimentally, we now verify the arguments predicted theoretically in Sec. II by the microwave scattering measurements using the vector network analyzer (VNA) at 50 mK.

First, under a sufficiently low dc-current bias such as, typically, $I_b = 0$, we had argued that the CBJJ device should behave as a boson-type macroscopic particle, i.e., a quantized linear harmonic oscillator. As a consequence, a peak of the measured transmitted spectrum of the applied traveling-wave microwave photons should be located at the plasma frequency ω_p , at which the phase shift of the transmitted wave should be zero. It is clearly shown in Fig. 11 that the argument is confirmed, i.e., the measured peak in the transmitted spectrum is revealed at $\omega_p/2\pi = 2.5949$ GHz. The measured quality factor reads $Q_{I_b=0} = 507$, which is approximated to the numerical simulation shown above. Also, the measured phase

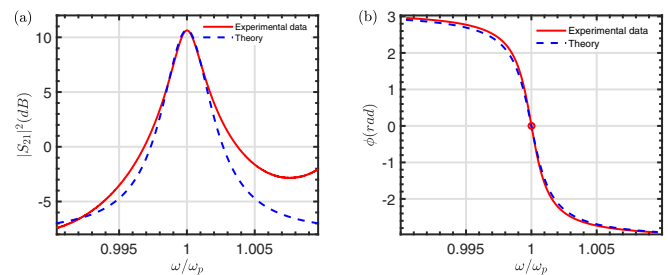


FIG. 11. The transmitted and phase shift spectra of the traveling-wave photons scattered by the CBJJ without the dc-current bias. (a) The transmitted spectrum with the peak at $\omega_p/2\pi = 2.5949$ GHz and the quality factor $Q = 507$. (b) The phase shift spectrum, in which the π phase is shifted at $\omega = \omega_p$. Here, the red line represents the measured results and the blue lines are the fittings from the theoretical calculations. The power of the driving microwave is $P = -80$ dBm (i.e., under the low-excitation limit) and the fitted parameters are set as $\kappa_1 = 0.004$ and $\kappa_2 = 0.008$.

shift of the transmitted wave at the frequency $\omega = \omega_p$ is really zero.

Second, let us check experimentally if the quantized CBJJ device with sufficiently large dc-current bias can serve as a fermion-type macroscopic particle. For sufficiently large dc-current bias, such as $I_b = 0.95 \mu\text{A}$ with $I_b/I_c = 0.97$, Fig. 12 shows the relevant transmitted and phase shift spectra of the traveling wave scattered by the device. It is seen clearly that the spectra are very different from those for the device with low current biases. Here, the resonant photons are reflected completely and the phase shift shows a transition behavior at the resonant point. This is the manifest feature of the traveling-wave photons scattered by a two-level atom (i.e., a fermion) predicted theoretically in Sec. II. The fitted data show that the eigenfrequency of the fermion (i.e., the two-level artificial atom) is $\omega_{01}/2\pi = 2.4182$ GHz, which is significantly less than $\omega_p/2\pi$ observed previously. The effective junction capacitance is $C'_J = 11.18$ pF, which is larger than C_J estimated previously in the absence of the dc-current bias. With the fitted data shown in Fig. 12, the critical current of the CBJJ without the current bias can be fitted as $I_c = 0.979 \mu\text{A}$, which is consistent with the one estimated by the

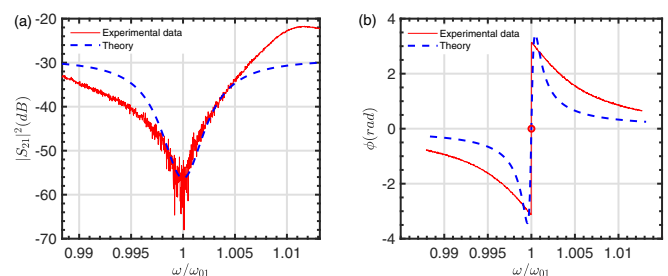


FIG. 12. The transmitted and phase shift spectra of the traveling-wave photons scattered by the CBJJ with the dc-current bias $I_b = 0.97I_c$. (a) The transmitted spectrum, and (b) the phase shift spectrum. Here, the power of the applied traveling wave is $P = -80$ dBm, the red lines represent the measured results, and the blue lines are fitted by the theoretical calculations with $\eta = 0.005$ and $\gamma = 0.0012$.

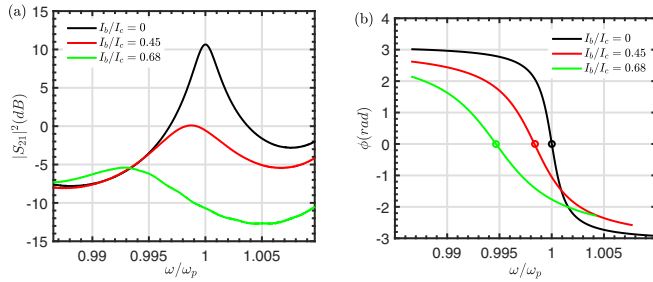


FIG. 13. The measured transmission of the traveling-wave photons scattered by the CBJJ with the dc-current biases being $I_b/I_c = 0$, 0.45, and 0.68, respectively. (a) The transmitted spectrum, and (b) the measured phase shift spectrum. Here, the drive power of the driving microwave is $P = -80$ dBm.

measured I - V curve. The quality factor of the device can be observed as $Q_b \sim 60$ for a significantly large dc-bias current. Also, the effective capacitance is calibrated as $C_f^j = 2.55$ pF in this case, which is larger than the junction capacitance C_j extracted by using the measured I - V curve, due to the effect of the parasitic capacitance under the high frequency drivings.

Immediately, beyond the extreme cases—i.e., the CBJJ working as either a boson under the bias $I_b = 0$ or a fermion under the bias $I_b/I_c \leq 1$ —the experimental measurements shown in Fig. 13 indicate that, with the increase of the bias dc current, the frequencies of the transmitted peaks are shifted left and also their relative heights decrease with the lower quality factors. Obviously, the stronger bosonic effect can be observed for the higher quality factors, if the CBJJ device is biased by the lower dc current. The asymmetric effects observed here on the transmitted peaks and phase shifts around the resonant point are due to the practically existing impedance mismatch between the CBJJ and the transmission line. This implies that the boson-type behavior is weakened. After that, if the biased current increases further, then a series of transmitted dips would appear, until a single dip was observed. This process refers to the increase of the fermion-

type behavior with enhanced quality factor and decreased resonant eigenfrequency. Certainly, the effective junction capacitance is changed if the CBJJ is biased by the different dc currents and is under high frequency driving.

IV. CONCLUSIONS AND DISCUSSIONS

In a realistic three-dimensional space, microscopic particles behave either as bosons satisfying the bosonic communication relation or fermions satisfying the fermionic communication one, respectively. Usually, due to the self-average, the physical behavior of macroscopic object is classical, except in certain extreme environments such as low temperatures. In this work we demonstrated experimentally that, under ultralow-temperature and low-power microwave driving, a current-biased macroscopic Josephson junction can serve as either a macroscopic “boson” particle or a macroscopic “fermion” one, depending on the amplitude of the biased dc current. As a consequence, the CBJJ device can be utilized in superconducting computing circuits to encode either a macroscopic qubit or work as the bosonic quantum data bus for coupling distant qubits and reading out the information of the qubit(s).

Hopefully, the macroscopic devices demonstrated here with controllable transformation between the bosonic and fermionic features can provide various applications for the simulations of quantum many-body physics [22–24], microwave single-photon detection [25–30], and also scalable quantum information processing [31–33], at macroscopic scale.

ACKNOWLEDGMENTS

This work is partially supported by the National Natural Science Foundation of China (NSFC) under Grant No. 11974290, and the National Key Research and Development Program of China (NKRDC) under Grant No. 2021YFA0718803.

-
- [1] A. Zee, *Quantum Field Theory in a Nutshell*, 2nd ed. (Princeton University Press, Princeton, 2010).
- [2] G. S. Canright and S. M. Girvin, Fractional statistics: Quantum possibilities in two dimensions, *Science* **247**, 1197 (1990).
- [3] H. Bartolomei, M. Kumar, R. Bisognin, A. Marguerite, J.-M. Berroir, E. Bocquillon, B. Plaçais, A. Cavanna, Q. Dong, U. Gennser, Y. Jin, and G. Fève, Fractional statistics in anyon collisions, *Science* **368**, 173 (2020).
- [4] C. Nayak, S. H. Simon, A. Stern, M. Freedman, and S. D. Sarma, Non-Abelian anyons and topological quantum computation, *Rev. Mod. Phys.* **80**, 1083 (2008).
- [5] M. Banerjee, M. Heiblum, V. Umansky, D. E. Feldman, Y. Oreg, and A. Stern, Observation of half-integer thermal Hall conductance, *Nature (London)* **559**, 205 (2018).
- [6] Y. Kasahara, T. Ohnishi, Y. Mizukami, O. Tanaka, S. Ma, K. Sugii, N. Kurita, H. Tanaka, J. Nasu, Y. Motome, T. Shibauchi, and Y. Matsuda, Majorana quantization and half-integer thermal quantum Hall effect in a Kitaev spin liquid, *Nature (London)* **559**, 227 (2018).
- [7] A. Y. Kitaev, Fault-tolerant quantum computation by anyons, *Ann. Phys. (NY)* **303**, 2 (2003).
- [8] T. I. Andersen *et al.* (Google Quantum AI and Collaborators), Non-Abelian braiding of graph vertices in a superconducting processor, *Nature (London)* **618**, 264 (2023).
- [9] M. Albiez, R. Gati, J. Fölling, S. Hunsmann, M. Cristiani, and M. K. Oberthaler, Direct observation of tunneling and nonlinear self-trapping in a single bosonic Josephson junction, *Phys. Rev. Lett.* **95**, 010402 (2005).
- [10] L. F. Wei, Y. Liu, and F. Nori, Quantum computation with Josephson qubits using a current-biased information bus, *Phys. Rev. B* **71**, 134506 (2005).
- [11] J. Clarke, A. N. Cleland, M. H. Devoret, D. Esteve, and J. M. Martinis, Quantum mechanics of a macroscopic variable: The phase difference of a Josephson junction, *Science* **239**, 992 (1988).

- [12] J. M. Martinis, S. Nam, J. Aumentado, and C. Urbina, Rabi oscillations in a large Josephson-junction qubit, *Phys. Rev. Lett.* **89**, 117901 (2002).
- [13] A. J. Berkley, H. Xu, R. C. Ramos, M. A. Gubrud, F. W. Strauch, P. R. Johnson, J. R. Anderson, A. J. Dragt, C. J. Lobb, and F. C. Wells, Entangled macroscopic quantum states in two superconducting qubits, *Science* **300**, 1548 (2003).
- [14] A. Blais, A. M. van den Brink, and A. M. Zagoskin, Tunable coupling of superconducting qubits, *Phys. Rev. Lett.* **90**, 127901 (2003).
- [15] J. A. Blackburn, M. Cirillo, and N. Grønbech-Jensen, A survey of classical and quantum interpretations of experiments on Josephson junctions at very low temperatures, *Phys. Rep.* **611**, 1 (2016).
- [16] M. J. Collett, and C. W. Gardiner, Squeezing of intracavity and traveling-wave light fields produced in parametric amplification, *Phys. Rev. A* **30**, 1386 (1984).
- [17] S. Boutin, D. M. Toyli, A. V. Venkatramani, A. W. Eddins, I. Siddiqi, and A. Blais, Effect of higher-order nonlinearities on amplification and squeezing in Josephson parametric amplifiers, *Phys. Rev. Appl.* **8**, 054030 (2017).
- [18] S. R. He, Y. F. Li, and L. F. Wei, Group delay controls of the photons transmitting through two cavities coupled by an artificial atomic ensemble: Controllable electromagnetically induced transparency-like effects, *Opt. Express* **30**, 721 (2022).
- [19] B. Yurke, Input-Output Theory, in *Quantum Squeezing* (Springer, Berlin, 2004), pp. 53–96.
- [20] S. Fan, Ş. E. Kocabaş, and J.-T. Shen, Input-output formalism for few-photon transport in one-dimensional nanophotonic waveguides coupled to a qubit, *Phys. Rev. A* **82**, 063821 (2010).
- [21] V. Ambegaokar and A. Baratoff, Tunneling between superconductors, *Phys. Rev. Lett.* **10**, 486 (1963).
- [22] D. J. Luitz and F. Piazza, Exceptional points and the topology of quantum many-body spectra, *Phys. Rev. Res.* **1**, 033051 (2019).
- [23] W. Kirkby, Y. Yee, K. Shi, and D. H. J. O’Dell, Caustics in quantum many-body dynamics, *Phys. Rev. Res.* **4**, 013105 (2022).
- [24] H. Atanasova, L. Bernheimer, and G. Cohen, Stochastic representation of many-body quantum states, *Nat. Commun.* **14**, 3601 (2023).
- [25] Y.-F. Chen, D. Hover, S. Sendelbach, L. Maurer, S. T. Merkel, E. J. Pritchett, F. K. Wilhelm, and R. McDermott, Microwave photon counter based on Josephson junctions, *Phys. Rev. Lett.* **107**, 217401 (2011).
- [26] A. Poudel, R. McDermott, and M. G. Vavilov, Quantum efficiency of a microwave photon detector based on a current-biased Josephson junction, *Phys. Rev. B* **86**, 174506 (2012).
- [27] I. Iakoupov, Y. Matsuzaki, W. J. Munro, and S. Saito, Sequential nonabsorbing microwave single-photon detector, *Phys. Rev. Res.* **2**, 033238 (2020).
- [28] G. H. Lee, D. K. Efetov, W. Jung, L. Ranzani, E. D. Walsh, T. A. Ohki, T. Taniguchi, K. Watanabe, P. Kim, D. Englund, and K. C. Fong, Graphene-based Josephson junction microwave bolometer, *Nature (London)* **586**, 42 (2020).
- [29] E. D. Walsh, W. Jung, G.-H. Lee, D. K. Efetov, B.-I. Wu, K.-F. Huang, T. A. Ohki, T. Taniguchi, K. Watanabe, P. Kim, D. Englund, and K. C. Fong, Josephson junction infrared single-photon detector, *Science* **372**, 409 (2021).
- [30] D. S. Golubev, E. V. Il’ichev, and L. S. Kuzmin, Single-photon detection with a Josephson junction coupled to a resonator, *Phys. Rev. Appl.* **16**, 014025 (2021).
- [31] G. Wendin, Quantum information processing with superconducting circuits: A review, *Rep. Prog. Phys.* **80**, 106001 (2017).
- [32] A. Blais, S. M. Girvin, and W. D. Oliver, Quantum information processing and quantum optics with circuit quantum electrodynamics, *Nat. Phys.* **16**, 247 (2020).
- [33] T. Hillmann, and F. Quijandría, Designing Kerr interactions for quantum information processing via counterrotating terms of asymmetric Josephson-junction loops, *Phys. Rev. Appl.* **17**, 064018 (2022).